International Journal of Fatigue 192 (2025) 108714

Contents lists available at ScienceDirect

International Journal of Fatigue

journal homepage: www.elsevier.com/locate/ijfatigue

Factors determining the torsional fatigue strength in bainitic steels with banded microstructures

Soma Yoshimura [a], Kentaro Wada [b], Sungcheol Park [c,*], Hisao Matsunaga [c,d]

[a] Graduate School of Engineering, Kyushu University, Fukuoka 819-0395, Japan
[b] National Institute for Materials Science (NIMS), Tsukuba 305-0047, Japan
[c] Research Center for Hydrogen Industrial Use and Storage (HYDROGENIUS), Kyushu University, Fukuoka 819-0395, Japan
[d] Department of Mechanical Engineering, Kyushu University, Fukuoka 819-0395, Japan

ARTICLE INFO

Keywords:
Bainitic steel
Banded microstructure
Torsional fatigue strength
Small crack
Finite element analysis

ABSTRACT

This study aimed to identify the microstructural factors governing the torsional fatigue strength of bainitic steels. Torsional fatigue tests were performed on two bainitic steels with banded microstructures comprised of soft and hard layers. The soft layers were coarse-grained with low Vickers hardness (*HV*), while the hard layers were fine-grained with high *HV*. Both materials possessed similar average *HV* values but differing band morphologies: a coarse band (CB) with $HV = 329$ and a fine band (FB) with $HV = 314$. Interestingly, the FB exhibited a 30 % higher fatigue strength than the CB. Through microscopic observations and finite element analysis, it was established that different fatigue strengths could be attributed to the particular width and array of the bands. The reticular band array in the FB steel raises crack initiation resistance due to the constraint of cyclic plastic deformation. In addition, the narrower spacing of hard layers can impede crack propagation when the extension mode transitions from shear mode to Mode I. In contrast, the columnar array and wider spacing of the bands in the CB steel are likely to provide weaker resistance to crack initiation and propagation, resulting in an inferior fatigue strength.

1. Introduction

In response to stringent CO_2 emission regulations and a growing emphasis on energy conservation, the marine industry has experienced a surge in demand for large engines capable of higher output and efficiency [1]. This has led to the need for engines with greater torque, thereby imposing increased torsional loads on power transmission shafts. Bainitic steels are emerging as promising candidates for the next generation of shaft materials, owing to their advantageous properties such as favorable strength-to-weight ratio and fracture toughness [2–4]. The high strength and toughness of these materials are mainly attributed to the elevated dislocation density in bainitic ferrite and the compact crystallographic boundaries in blocks and packets of bainitic ferrite [5].

To date, extensive research has been primarily focused on exploring the relationship between microstructures and mechanical properties, with the aim of developing advanced bainitic steels that offer enhanced strength [6–9]. However, in order for the full potential of bainitic steels to be realized in industrial applications (such as power transmission shaft systems where components commonly undergo cyclic loading), a deeper understanding of their fatigue behavior is indeed essential. While several research groups have studied the fatigue response of bainitic steels with diverse morphologies in the low-cycle fatigue regime [10–14], the behavior of fatigue cracks in the high-cycle regime, especially near the fatigue limit, is still not fully understood.

It is generally believed that the fatigue limit of metallic materials should be treated as a small-crack problem [15]. Through a series of experiments involving various ferrous alloys (including some aluminum and copper alloys), Murakami *et al.* [15] demonstrated that the fatigue limit is not the critical condition where no crack initiates, but the threshold condition at which Mode I small cracks cease propagation. Based on the experimental findings, they proposed a fracture mechanics-based, $\sqrt{area}$ parameter model [16]. In this model, Vickers hardness (*HV*) is incorporated as a microstructural factor to account for the growth resistance of small cracks on the fatigue limit. Many researchers have attempted to validate the efficacy of this model while quantitatively assessing the fatigue strength of materials exhibiting Mode I, small-crack growth behavior at the fatigue limit [17–19].

On the other hand, there is a dearth of research with regard to the

* Corresponding author at: Research Center for Hydrogen Industrial Use and Storage (HYDROGENIUS), Kyushu University, Fukuoka 819-0395, Japan.
E-mail address: park.sungcheol.982@m.kyushu-u.ac.jp (S. Park).

https://doi.org/10.1016/j.ijfatigue.2024.108714
Received 11 July 2024; Received in revised form 13 November 2024; Accepted 14 November 2024
Available online 17 November 2024

behavior of small cracks under repeated shear loading, such as cyclic torsion. In shear-mode crack-growth, the impacts of crack-face interactions, *e.g.*, friction, abrasion and/or mechanical locking of asperities, are known to be crucial [20–22]. For example, Okazaki *et al.* [23] established that the shear-mode threshold of a bearing steel (SAE52100) was diminished with an increase in static crack-opening stress (*i.e.*, with reduced crack-face interference). More recently, Tanaka *et al.* [24] conducted three types of fatigue tests (push–pull, pure torsion and torsion superposed with static tensile stress) to explore the influence of crack-opening/-closing stresses on the shear-mode threshold of Ni-based superalloy 718. In contrast to the finding by Okazaki *et al.*, the shear-mode threshold of the alloy was rarely affected by static, crack-opening/-closing stresses. These results were ascribed to the relatively straight/short morphologies of arrested cracks, leading to the lesser influence of mechanical locking and frictional resistance of crack-faces. In addition to the mechanical factors, several researchers have emphasized that the propagation and arrest behaviors of small, shear-mode fatigue cracks are significantly influenced by microstructural features, such as crystallographic orientation or secondary-phase particles near the crack-tip [25,26]. Given the complex microstructure of bainitic steel and in view of its potential application in various shaft systems, it is vital to identify the microstructural factors that affect the propagation behavior of small, shear-mode fatigue cracks in the material under cyclic-shear loading conditions.

To the best of the authors' knowledge, there are no existing studies examining the impact of microstructure on the small fatigue-crack behavior of bainitic steels under cyclic torsional loading near the fatigue limit regime. Therefore, we investigated torsional fatigue strengths of two types of bainitic steels with dissimilar microstructural morphologies, but comparable *HV*. The test results revealed a difference of approximately 30 % in the torsional fatigue strength in a high-cycle regime. Through quantitative examination *via* electron microscope, hardness measurement and finite element analysis (FEA), it was concluded that such a variance can be credited to disparities in the spacing and arrays of the banded microstructures.

2. Materials and methods

2.1. Materials

The experimental materials consisted of two types of bainitic steels under consideration for marine propulsion shaft applications. Both materials shared the chemical composition of 0.4C-1Cr-0.5Mo (wt.%). Fig. 1 exhibits the optical microscope images obtained using Nital and Picral etchings, revealing banded microstructures in each material. Both materials feature alternating fine-grained and coarse-grained areas

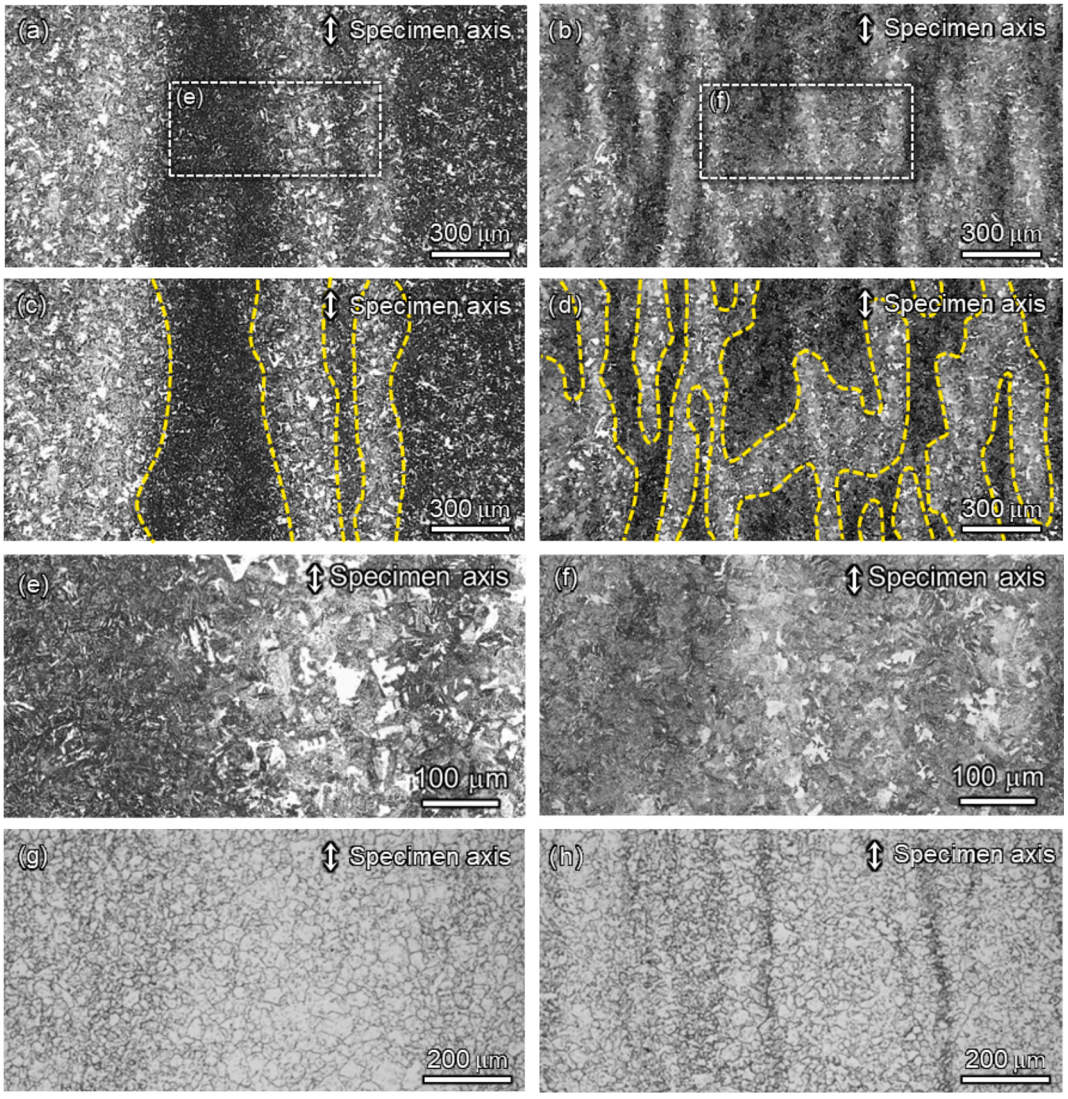

Fig. 1. Optical microscope images of the microstructures in two bainitic steels obtained by (a) ~ (f) Nital etching; (g)(h) Picral etching. CB material = (a)(c)(e)(g); FB material = (b)(d)(f)(h).

elongated in the axial direction. It should be noted that the images in Fig. 1(c) and (d), in which the band boundaries are denoted by dotted yellow lines, correspond to those in Fig. 1(a) and (b), respectively. After comparing these microstructures, a distinct difference was observed in the widths of the band structures. Hereafter, materials with wider bands (*cf*. Fig. 1(a),(c),(e) and (g)) are referred to as coarse-band (CB) materials, whereas those with narrower bands (*cf*. Fig. 1(b),(d),(f) and (h)) are termed fine-band (FB) materials. The average spacing of band structures was 455 μm for CB materials and 175 μm for FB materials. In addition to the band spacing, the array of the band structure varies according to the material, *i.e.*, CB materials displayed a columnar band structure, whereas reticular band structures were found in FB materials (*cf*. Fig. 1(c) and (d)). The singularity of these microstructures is accredited to distinct cooling rates, *i.e.*, the FB material was obtained by a faster cooling rate than the CB material. Table 1 presents the mechanical properties of the materials, including *HV*, 0.2 % proof stress ($\sigma_{0.2}$), tensile strength (σ_B) and reduction in area (φ). The hardness values were derived from 50-points along a straight line with a spacing of 100 μm, measured with a load of 0.98 N and a holding time of 10 s (indentation dimensions: approximately 20 ~ 25 μm). Both CB and FB materials registered similar average *HV* values.

The characteristics of the banded microstructures identified in Fig. 1 were further analyzed by Electron Backscatter Diffraction (EBSD) and Energy Dispersive X-ray Spectroscopy (EDX) techniques, using a JEOL JSM-7001F scanning electron microscope (SEM) with an acceleration voltage of 20 kV (a beam step-size of 0.2 ~ 0.4 μm) and 15 kV, respectively. Furthermore, to clarify the difference in microscopic hardness between the fine-grained and coarse-grained regions of these materials, *HV* distribution was measured on the circumferential and axial cross-sections of both the CB and FB materials. After the measurements, the areas surrounding the indentations were subjected to Nital etching to investigate the relationship between hardness and microstructure.

2.2. Finite element analysis

The *HV* measurements revealed an apparent deviation in *HV* values between fine-grained regions and coarse-grained regions (*cf*. Section 3.1). This indicates that the materials investigated in this study possessed soft and hard layers, similar to a dual-phase material. Moreover, CB and FB materials have dissimilar band arrays, *i.e.*, columnar band and reticular band structures, respectively. In order to determine the influence of the banded microstructure array on the stress and plastic strain state under torsional loading, elasto-plastic FEA was performed using the Abaqus CAE 2021, as will be examined later in Section 4.3.

Two-dimensional models with varying band arrays were generated, as illustrated in Fig. 2. In the figure, light gray and dark gray correspondingly represent the soft and hard layers. For the reticular band configuration, aspect ratios, AR = a/W, of 2.5, 5 and 10 were chosen for FEA. In most analysis cases with a dimension of $B = 25\ W$, the model consisted of 63,001 nodes and 62,500 elements, with the exception of the AR = 10 case which necessitated 251,001 nodes and 250,000 elements due to the larger dimensions of the model ($B = 50\ W$). The 4-node, plane stress element (CPS4R) was employed for all simulations. Remote shear stress was set at 453 MPa to ensure that the maximum resultant plastic strain remained below 0.3 %, a reasonable value near the fatigue limit regimes. To prohibit the discontinuous deformation, a rigid body constraint was applied at the top and bottom of the model, as indicated by the solid blue lines in Fig. 2.

Table 1
Mechanical properties of experimental materials.

Material	*HV*	$\sigma_{0.2}$ [MPa]	σ_B [MPa]	φ [%]
CB	329	895	1064	56.0
FB	314	869	1033	70.6

For material properties, Young's modulus ($E = 206$ GPa) and Poisson's ratio ($\nu = 0.3$) were utilized in the elastic deformation regime. The true stress–strain curve for FEA was derived based on the mechanical properties obtained from tensile testing. It should be noted that, considering the ≈ 20 % difference in *HV* between two layers, the yield strengths of the soft and hard layers were determined to be 782 MPa and 978 MPa, respectively. Fig. 3 plots the relationship between true stress and true strain as used in the FEA.

2.3. Torsional fatigue tests

Cylindrical specimens with diameters of 5 mm and gauge section lengths of 25 mm were fabricated for the torsional fatigue tests, ensuring the alignment of the specimen axes with the direction of the shaft axes. All specimen surfaces were polished with emery papers, followed by buffing with a diamond paste. The shape and dimensions of the specimens are illustrated in Fig. 4. Torsional fatigue tests were then conducted with a resonance fatigue-testing machine, operated at a stress ratio, R, of -1 and a test frequency, f, of 45 ~ 50 Hz. In this study, the torsional fatigue limit was defined by the shear-stress amplitude, τ_a, at which a specimen did not fail after loading at 10^7 cycles, even though the limited number of tests could not precisely determine the fatigue limit in accordance with the relevant standards. All tests were carried out in ambient air at room temperature and, periodically, were halted to examine the propagation of fatigue cracks, using the plastic replica method. Following the fatigue tests, the microstructures surrounding the surface cracks were analyzed using EBSD, in order to elucidate the relationship between crack initiation/propagation behavior and the microstructures. The observation conditions were maintained consistent with those described in Section 2.1.

3. Results

3.1. Microscopic observations

The initial microstructures of the CB and FB materials obtained through EBSD are showcased in Fig. 5. Inverse pole figure (IPF) maps are presented in Fig. 5(a),(d),(g) and (j), with grain boundary (GB) maps displayed in Fig. 5(b),(e),(h) and (k). In this context, a GB was established as being the boundary between regions misoriented by more than 15°. As was the case in Fig. 1, Fig. 5 also confirms the presence of a banded microstructure consisting of coarse-grained and fine-grained regions. It is noted that Fig. 5(g) ~ (i) and Fig. 5(j) ~ (l) correspond to coarse-grained and fine-grained regions in CB material, respectively. Furthermore, as illustrated in Fig. 5(c),(f),(i) and (l), no significant disparity in GB misorientation angle distribution was detected in either the CB or FB materials and either coarse-grained or fine-grained regions.

Fig. 6 features the elemental mapping obtained *via* EDX for the CB and FB materials. Due to the detection limits of the equipment, the carbon distribution could not be ascertained during analysis of all the samples. Conversely, it was clearly observed that Cr and Mn were distributed in a banded manner within specific zones of all materials. The width of these bands in the FB material ranged from 100 to 300 μm, closely corresponding to the width of the banded structures observed in Fig. 1. Therefore, it can be inferred that the micro-segregation of these alloying elements is strongly related to the formation of banded structures in both CB and FB materials.

In general, bainite exhibits a hierarchical structure of packets, blocks, and laths within the prior austenite GBs, similar to that of lath martensite [27]. However, upon examination *via* EBSD, such fine hierarchical structures were not perceived in the coarse-grained regions of the CB and FB materials, whereas they were distinctly present in the fine-grained regions (*cf*. Fig. 5(g),(h),(i) and (k)). It is also accepted that the addition of alloying elements such as Cr, Nb, Mo and B enhances the hardenability of steel, thus ensuring the transformation to bainite/martensite during the quenching process which in turn refines the

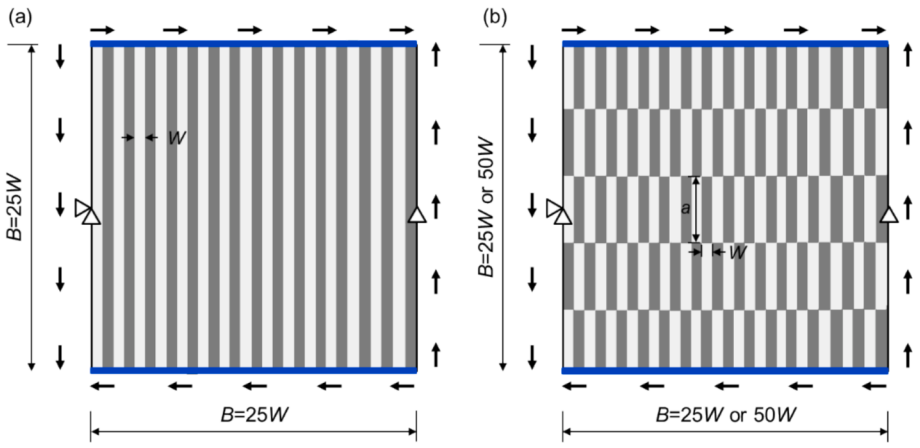

Fig. 2. Representation of FEA models with different band morphologies: (a) columnar band; (b) reticular band.

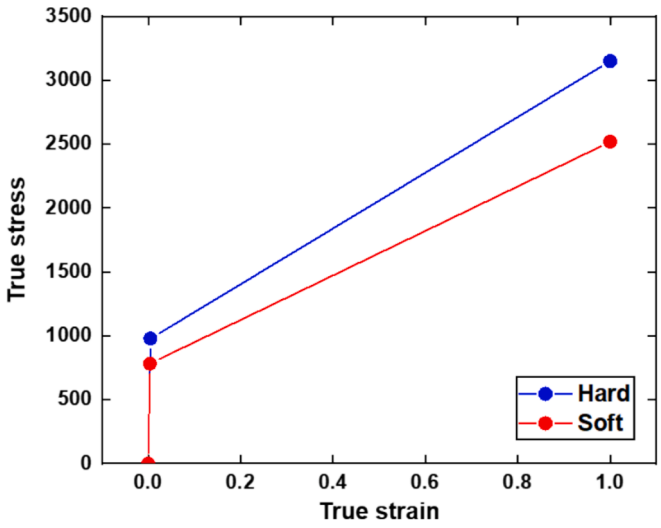

Fig. 3. True stress and true strain curves for FEA.

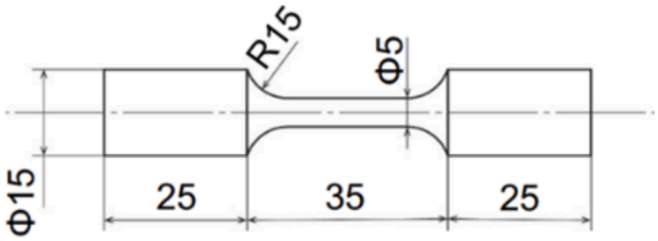

Fig. 4. Shape and dimensions of torsional fatigue test specimens (mm).

microstructure [28,29]. For example, Ali *et al.* [30] examined the impact of varying Cr content (1 wt% ~ 4 wt%) on the microstructure and mechanical properties of hot-rolled, low-carbon (0.04 wt%) steel plates. Their findings revealed that higher Cr concentrations boosted hardenability, thereby not only promoting the formation of bainite, but also significantly refining the microstructure. Therefore, in this study, it is believed that the segregation of alloying elements such as Cr and Mn resulted in uneven hardenability within the materials, ultimately leading to a banded structure characterized by a mixture of coarse-grained and fine-grained regions.

3.2. Vickers hardness distribution

The results of hardness distribution measurements are detailed in Fig. 7, together with those of microstructural observations by optical microscope on areas surrounding the indentations after Nital etching. The circumferential and axial sections of CB and FB materials are depicted in Fig. 7(a) ~ (d). In each image, the average *HV* values are indicated by straight lines. Additionally, figure insets display the indentations representing the minimum and maximum *HV* values from among 50 measurement points, correspondingly labeled as A1 to D1 and A2 to D2.

When comparing the microstructures surrounding indentations with the maximum and minimum *HV* values in Fig. 7(a) ~ (d), the lowest *HV* was consistently measured in the coarse-grained regions, whereas the highest *HV* was recorded in the fine-grained regions, across all cross-sectional positions in both materials. Moreover, it was observed that regions with high and low *HV* values were alternately distributed in all materials. The average periodicities for the alternation in the circumferential and axial sections were approximately 400 μm and 650 μm for the CB material, 200 μm and 280 μm for the FB material, respectively. These values closely correspond to the band-spacing between coarse-grained and fine-grained regions mentioned in Section 2.1. Therefore, it is confirmed that the spacing between coarse-grained and fine-grained regions is approximately 2 to 3 times wider in CB material than in FB material.

3.3. Fatigue test results

The *S-N* data obtained by the torsional fatigue tests is displayed in Fig. 8. The results for the CB material are represented by solid orange circles, while those for the FB material are depicted by solid blue diamonds. The torsional fatigue limits for CB and FB materials are 230 MPa and 310 MPa, respectively. It is interesting to note that, despite having equivalent *HV* values, these materials exhibit a difference of approximately 30 % in fatigue limit. The proportional relationship between fatigue limit and *HV*, commonly observed during the tension–compression fatigue testing of steels [31], was not valid in this case.

As mentioned in the introductory section, it is commonly known that the fatigue limit is determined by the threshold condition of small fatigue cracks. A similar phenomenon was also discovered in the present study, *i.e.*, multiple, arrested small cracks were detected at the fatigue limit of the FB material, although no arrested cracks were found in the CB material. Optical microscope images of the arrested cracks discerned in the FB specimen tested at the fatigue limit (τ_a = 310 MPa) are displayed in Fig. 9(a) ~ (d), while Fig. 9(e) and (f) correspondingly portray an IPF map and a GB map of the crack. It should be noted that cracks in

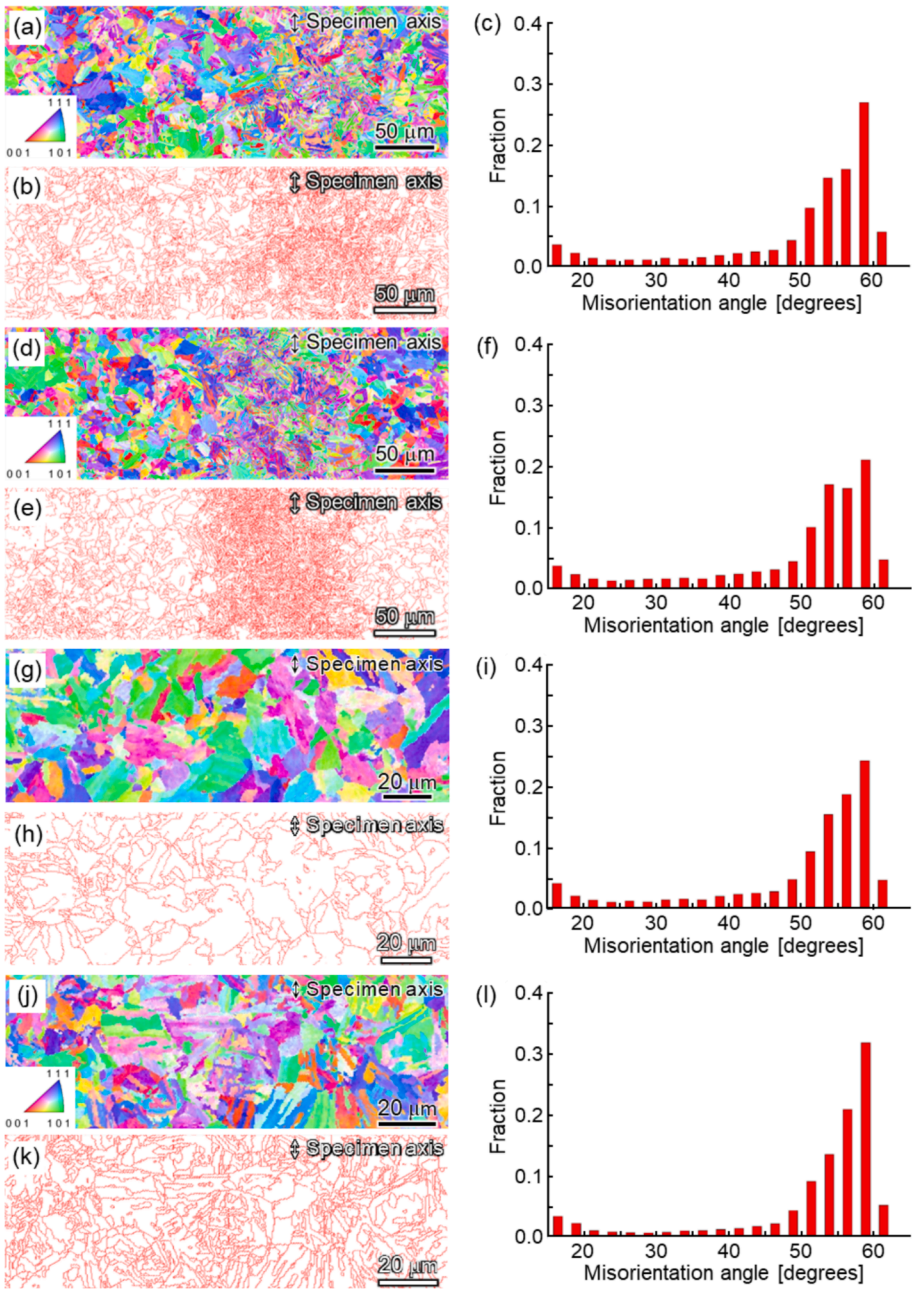

Fig. 5. Initial microstructures of bainitic steels: IPF map, GB map and GB misorientation angle distribution for (a) ~ (c): CB; (d) ~ (f): FB; (g) ~ (i): coarse-grained region in CB; (j) ~ (l): fine-grained region in CB.

the FB material initiated in the coarse-grained regions. Moreover, the cracks mainly propagated along paths parallel to the {110} planes, one of the slip planes of BCC metal, as indicated by the straight blue lines in Fig. 9(f).

A higher magnification of the IPF maps and SEM images associated with the arrested crack in FB (*cf.* Fig. 9(a)) is presented in Fig. 10. Fig. 10 (a) ~ (c) corresponds to the regions near the crack-initiation site, while the areas near the branched crack-tip are displayed in Fig. 10(d) ~ (f). The featured grains are labeled, with each {110} plane trace highlighted by different colors. Considering that crystallographic, small fatigue-cracking was prominent near the threshold condition in this material, the influence of GB misorientation should play a critical role in the fatigue crack-growth/-arrest mechanism. According to Zhai *et al.* [32], two geometric parameters of crack-planes between neighboring grains, *i.e.*, the twist angle and the tilt angle, should be considered when interpreting the crystallographic cracking behavior. The calculated twist angles (α) and tilt angles (β), along with the maximum Schmid factors (SFs) for each {110} slip plane, are provided in Table 2. The active slip systems, *i.e.*, the crack-planes adjacent to GBs, have been emphasized in bold font. It must be pointed out that the precondition for crack-growth across GBs was not only the presence of slip planes with high SFs, but also those that demonstrate strong compatibility (low twist/tilt angles) in adjacent grains. In fact, the $(1\bar{1}0)$, (101), $(10\bar{1})$ and $(01\bar{1})$ planes in Grain 2 bore almost identical SF values, but the crack propagated along the $(1\bar{1}0)$ plane which possessed an advantageous geometrical relationship with the (110) plane in Grain 1. On the other hand, all of the twist angles in Grain 4 with respect to Grain 3 were significantly high, with the exception of the $(10\bar{1})$ plane with a substantially low SF, a plausible reason for crack-arrest in the vicinity of the GB between Grains 3 and 4. If the tilt angle was the most critical factor, the crack should have propagated along the $(01\bar{1})$ plane in Grain 4 with the highest SF

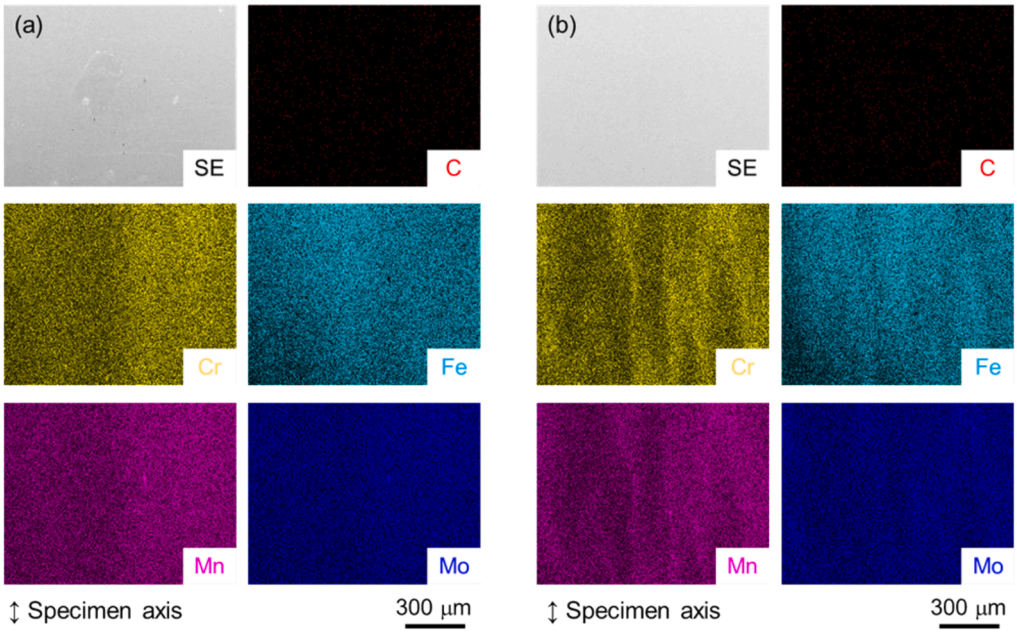

Fig. 6. Elemental mappings of C, Cr, Fe, Mn and Mo in (a) CB and (b) FB.

and the lowest tilt angle. These results suggest that the twist angle primarily influences the fatigue crack-growth and −arrest mechanism in this material, while the tilt angle plays a secondary role, echoing results of previous experimental studies using bainitic steels [10,13].

Fig. 11 illustrates two fatigue cracks propagating over hundreds of microns in FB material tested at $\tau_a = 320$ MPa, observed using an optical microscope. Different growth behaviors were registered by the two cracks. The crack in Fig. 11(a) propagated along the axial direction and subsequently branched into Mode I. This implies that in the initial stage of cracking, the fatigue crack propagated as a shear-mode crack in the axial direction (the direction of the maximum shear stress), then branched out in the direction of the principal stress. Conversely, the crack in Fig. 11(b) continued to grow in shear mode before it stopped propagating, an occurrence which will be discussed in a later section.

Fig. 12 illustrates the non-fatal crack that did not contribute to final fracture in the broken CB specimen tested at $\tau_a = 300$ MPa. Just like the arrested cracks in the FB material, this crack also initiated and grew along a direction parallel to the {110} plane. The plastic replica observation of a crack propagating in CB material at $\tau_a = 280$ MPa is showcased in Fig. 13(a) ~ (d). The shear-mode cracks initiated along the axial direction of the specimen and then grew in a few hundred microns. EBSD examination later revealed that the crack originally initiated in the coarse grain and propagated along a direction nearly parallel to the {110} plane, as indicated by the solid blue line (*cf.* Fig. 13(e) and (f)). Subsequently, it branched in an oblique direction at $N \approx 3.7 \times 10^5$ cycles, leading to the final fracture. The results infer that, once initiated, the crack could not stop propagating in the CB material. This suggests the presence of dominant mechanisms for various fatigue limits between CB and FB materials, an issue that will be discussed in the following section.

4. Discussion

The preceding results highlight the inferior fatigue-crack resistance of CB materials when compared to that of FB materials, in spite of their similar mechanical properties, as outlined in Table 1. In addition, both materials exhibited a common characteristic in cracking behavior, *i.e.*, fatigue cracks initiated within coarse grains and propagated along crystallographic slip planes. In a previous study by the authors [33], it was revealed that microstructural texture significantly affects the fatigue threshold of Ni-based superalloy 718, in which crystallographic crack propagation is predominant. However, both materials used in this study showed random crystal orientations in each coarse- and fine-grained region, as evidenced by the distribution of GB misorientation angles in Fig. 5(c) and (f). Meanwhile, Zhang *et al.* [34] explored the influence of a non-uniform microstructure resulting from alloying elemental segregation on the rolling contact fatigue strength of bainitic rail steel. Their findings revealed that fatigue crack propagation predominantly occurred along the segregation boundary. However, in contrast, no correlation between segregation boundaries and crack behavior was found in this study. Therefore, the inferior fatigue strength of the CB material should be attributed to factors other than microstructural texture and micro-segregation. In the following sections, some possible dominant factors will be further examined by focusing on (i) grain size, (ii) band spacing and (iii) band array.

4.1. Effect of grain size

As mentioned in the introduction, it is widely accepted that the fatigue limit relies greatly on the size of the initial defect and crack. As demonstrated in the previous section, cracks initiate within coarse grains in both the CB and FB materials. Furthermore, for these cracks, the GBs provided primary resistance to crack-growth. These results suggest that the size of initiated cracks is dependent on the maximum grain size in each material [17,35].

Since Murakami *et al.* [16] adopted extreme value statistics (EVS) to estimate maximum inclusions for quantitatively evaluating the effects of these inclusions on the fatigue limit, this statistical analysis has been widely used in the quality control of metallic materials which inevitably contain defects (*e.g.*, high-strength steels, cast irons, additively-manufactured materials, *etc.*) [36–39]. Recently, Kevinsanny *et al.* [40] demonstrated the effectiveness of using the maximum grain size (estimated using EVS) in the prediction of the lower bound of fatigue limit for additively-manufactured, Ni-based superalloy 718. Similarly, to examine the impact of the grain size on the fatigue limit, this study attempted to apply the EVS method to the prediction of the maximum grain sizes of CB and FB materials, potentially closely linked to crack-initiation sizes.

The gauge sections of both CB and FB specimens were embedded in phenolic resin, then polished with emery papers and later finished by

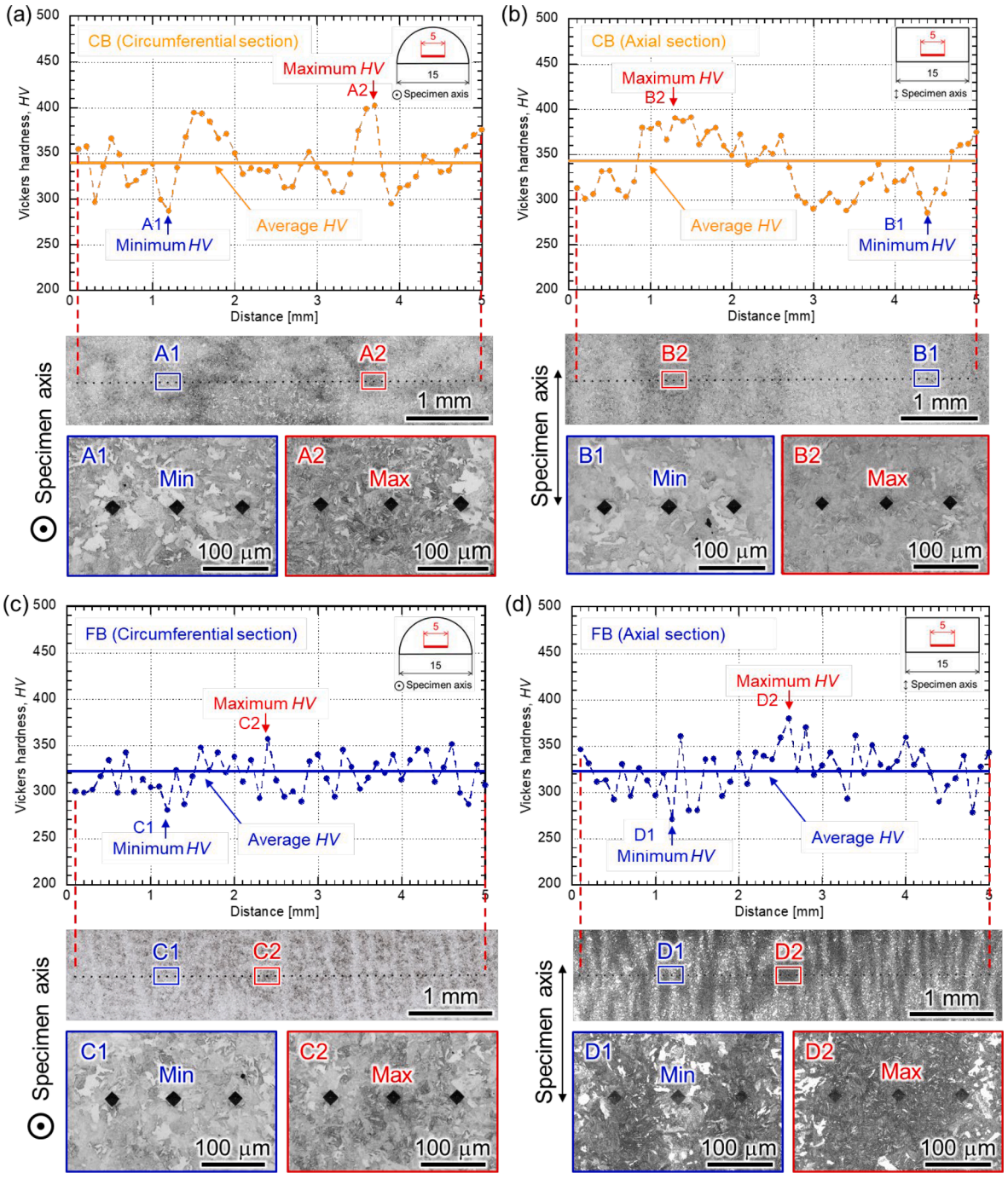

Fig. 7. Line profiles of *HV* in (a)(b): CB; (c)(d): FB.

buffing. Using the EBSD technique, microstructural images were collected after 20 separate inspections. The maximum grain size for each predefined inspection area measuring 2.18×10^{-2} mm^2 (the field of view at 1000 × magnification) was identified with the aid of the grain size measurement tool in OIM Analysis™ software. A GB was defined as the boundary between regions with a misorientation greater than 15°. The sampled data was then organized and displayed on a probability plot for extreme value distribution. Sample images and the values for the distribution of extremes for both materials are presented in Fig. 14. The linear distribution of the maximum grain size was determined using the least-squares method for both the CB and FB materials, respectively:

$$d_{max} = 6.52y + 29.2 \quad (1)$$

$$d_{max} = 7.66y + 31.1 \quad (2)$$

where, d_{max} is the predicted maximum grain size and y is the reduced variate. By entering the y value corresponding to the surface area of a specimen's gauge section into Eqs. (1) and (2), the d_{max} values were established to be 93 µm and 106 µm for CB and FB materials, respectively. Contrary to expectations, no substantial variance in the maximum grain sizes was observed between the two materials. Therefore, these results imply that the maximum grain size may not be a critical factor in the inferior fatigue strength of the CB material.

The reason for the similar maximum grain sizes in CB and FB materials can be explained as follows. Considering that fine hierarchical bainitic structures like blocks and packets are not observed within the coarse-grained regions of CB and FB materials, it is believed that the

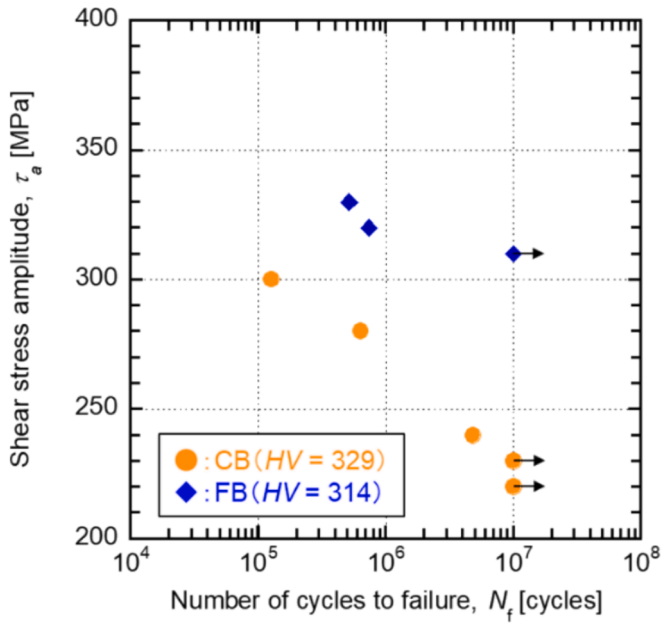

Fig. 8. *S-N* diagram of torsional fatigue testing of CB and FB materials.

grain sizes of these coarse-grained regions correspond to the prior austenite grain sizes. Meanwhile, the average prior austenite grain sizes of the CB and FB materials, as measured by the intercept method using optical microscope images of Picral-etched microstructures (*cf*. Fig. 1(g) and (h)), were 25 μm and 30 μm, respectively. Therefore, it was confirmed that the similarity in the estimated maximum grain sizes of both materials was due to their equivalent prior austenite grain sizes.

4.2. Effect of band spacing

It is generally accepted that inclusions, micro-defects or softer layers act as initiation sites for fatigue fractures, while microstructural features with higher strength provide resistance to the growth of small fatigue cracks. For instance, Endo and Yanase [41] confirmed that at the torsional fatigue limit of ferritic and pearlitic steels, cracks originating from the softer ferrite grains were arrested by the harder pearlite grains. In this study, the coarse-grained regions registered a hardness value approximately 100 *HV* units lower than that of the fine-grained regions, as illustrated in Fig. 7. Therefore, cracks were more likely to initiate and propagate in the coarser microstructure. However, it is interesting to note that although the FB material displayed a minimum hardness value about 30 *HV* units lower than that of the CB material, the fatigue limit of the FB material was higher than that of the CB material. This implies that the difference in fatigue limits cannot be solely attributed to the hardness values in the coarse-grained regions.

As described in Section 3.2, the spacing of the banded microstructure in the CB material was approximately 2 − 3 times larger than that of the FB material (*cf*. Fig. 7). Furthermore, coarse-grained regions serve as initiation sites for crack formation, whereas fine-grained regions resist crack propagation. Based on these macro/microscopic observations, fatigue failure in the CB material is believed to occur through the following process, as illustrated in Fig. 15(a). Firstly, cracks initiate along {110} slip planes in coarse-grained regions with lower *HV*. These cracks propagate in the axial or circumferential direction, where maximum shear stress occurs, and then may partially branch into Mode I. The transition from shear-mode to Mode I crack propagation could be imputed to the mechanical states near the crack-tip. Erdogan and Sih [42] demonstrated the correlation between $K_{I\theta max}$ and K_{IImax} at the tip of a Mode II crack in an infinite plane subjected to remote shear stress:

$$K_{I\theta max} = 1.15 K_{IImax} \tag{3}$$

where, $K_{I\theta max}$ and K_{IImax} are correspondingly the maximum Mode I and Mode II stress intensity factors (SIF). Equation (3) indicates that, even under solely remote shear stress (*i.e.*, Mode I SIF, $K_I = 0$, macroscopically), the local normal-stress field develops in the vicinity of the crack-tip so that the crack can propagate in Mode I. When the branched, Mode I crack reaches fine-grained regions, it encounters significant resistance to crack propagation due to higher *HV* [31]. However, the increased driving force, resulting from the crack propagating over a long distance, compels the crack to continue extending without being arrested, ultimately leading to fracture. This process may be consistent with the experimental observation that no arrested cracks were found in the CB material.

In the FB material, as depicted in Fig. 15(b), the processes of crack initiation and propagation in shear mode are believed to be similar to

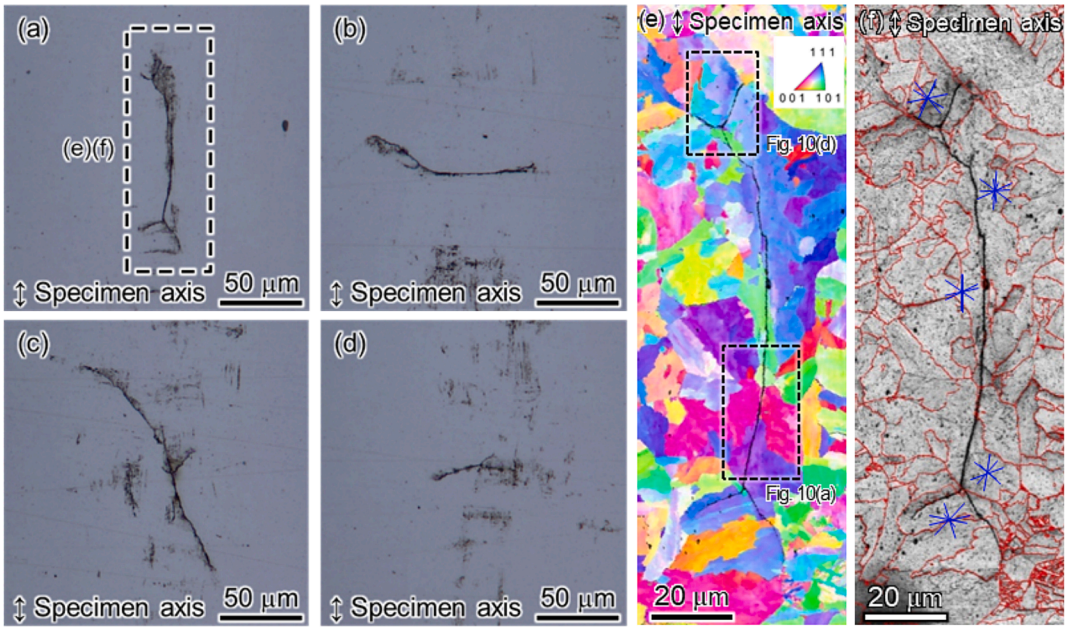

Fig. 9. Non-propagating cracks in FB tested at τ_a = 310 MPa: (a) ~ (d) Optical micrographs; (e) IPF map; (f) GB map.

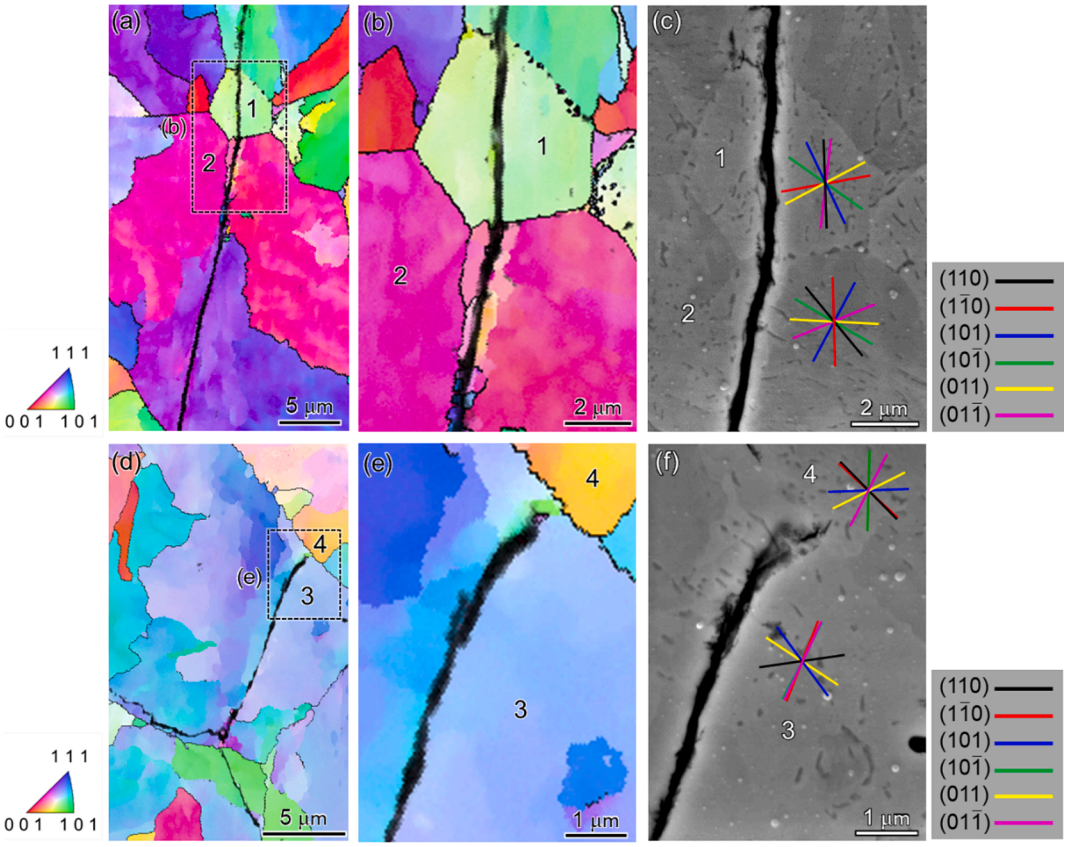

Fig. 10. IPF maps and SEM images of crack-growth/-arrest behaviors at the fatigue limit.

Table 2
Results of calculated SF, α and β values along crack-paths.

Grain	Slip planes	SF	α	β	Grain	Slip planes	SF	α	β
Grain 1	**110**	**0.25**	/	/	Grain 2	110	0.39	74	38
	1$\bar{1}$0	0.27				**1$\bar{1}$0**	**0.44**	**16**	**1**
	101	0.22				101	0.46	40	30
	10$\bar{1}$	0.37				10$\bar{1}$	0.44	3	58
	011	0.37				011	0.39	73	85
	01$\bar{1}$	0.47				01$\bar{1}$	0.46	35	69
Grain 3	110	0.19	/	/	Grain 4	110	0.43	47	70
	1$\bar{1}$0	0.20				1$\bar{1}$0	0.30	59	73
	101	0.49				101	0.14	95	63
	10$\bar{1}$	0.46				10$\bar{1}$	0.17	1	24
	011	0.47				011	0.44	51	38
	01$\bar{1}$	**0.39**				**01$\bar{1}$**	**0.44**	**58**	**2**

those in the CB material. However, since the spacing between the coarse- and fine-grained regions in the FB material is narrower, a crack branching into Mode I promptly reaches the fine-grained region with higher *HV*. Given that the Mode I crack-driving force is relatively smaller owing to the crack-growth over a shorter distance when compared to the CB material, Mode I cracks in FB material are likely to halt when they encounter the fine-grained region with higher crack-resistance. Simultaneously, the original shear-mode cracks experience a reduction in the driving force for propagation due to stress-field shielding by crack-branching. As a result, these cracks are unlikely to propagate further, in either Mode I or shear mode. It can also be speculated that under stress amplitudes exceeding the fatigue limit, the process repeats with (i) crack-branching into Mode I, (ii) arrest of the branched cracks and (iii) continued propagation in shear mode. This can account for the presence of a macroscopically long crack along the axial direction, accompanied by many tiny branched cracks, as featured in Fig. 11(b).

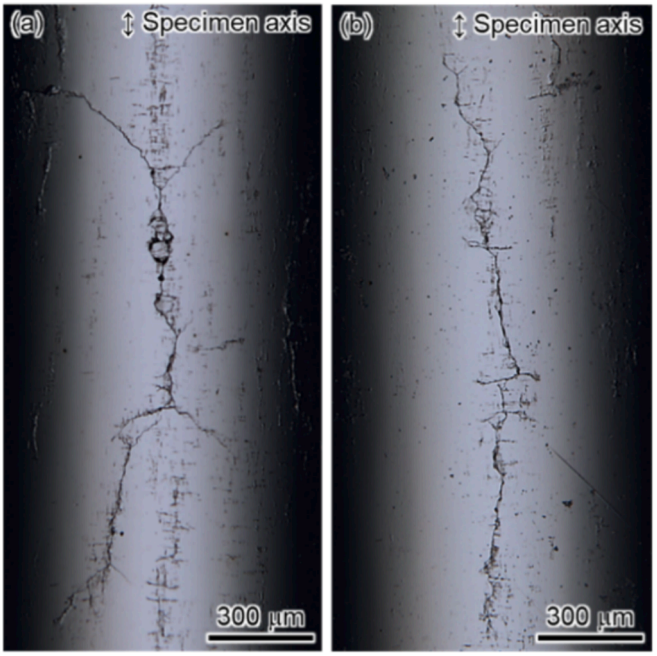

Fig. 11. Crack-propagation behavior in FB tested at τ_a = 320 MPa.

Consequently, the distinct fatigue limits between CB and FB materials can be linked to the dissimilar band spacing between the coarse-grained and fine-grained regions. In other words, the fatigue limit of CB material, characterized by relatively wider, coarse-grained regions

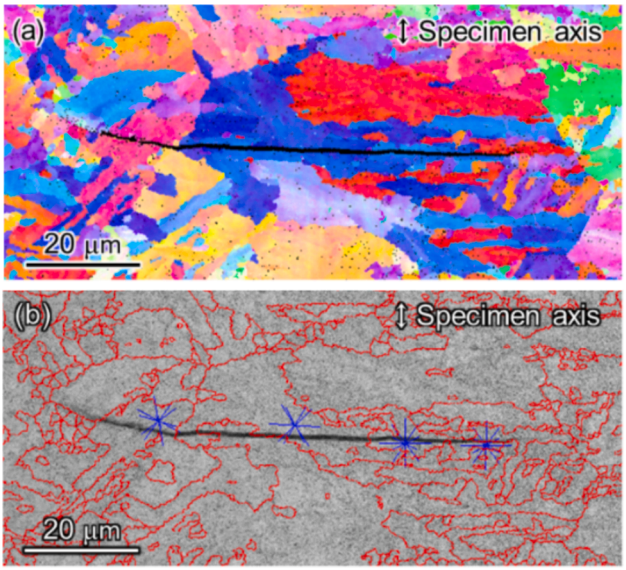

Fig. 12. EBSD observation of a non-fatal crack in the CB material, tested at τ_a = 300 MPa: (a) IPF map; (b) GB map.

with lower hardness, is determined by the threshold condition for crack initiation. On the other hand, the fatigue limit of FB material, which features relatively narrower, coarse-grained regions, is ruled by the threshold condition for crack propagation. Therefore, it should be emphasized that the band-spacing can be a critical factor governing the mechanism determining the fatigue limit in these materials.

4.3. Effect of band array

Although the spacing of banded microstructures is considered to be a crucial factor, as discussed in the previous section, this does not fully explain the experimental findings that some cracks in run-out FB specimens stopped their propagation in shear-mode without branching into Mode I. As mentioned in Section 2.1, microstructures show distinct band arrays between CB and FB materials, *i.e.*, columnar and reticular band structures, respectively. Accordingly, this section investigates the impact of band arrays on mechanical states within CB and FB materials when subjected to identical stress conditions.

Fig. 16(a) shows the shear stress distribution obtained *via* FEA for materials with diverse band arrays under remote shear stress, whereas Fig. 16(b) presents the plastic shear strain distribution. In these figures, soft and hard layers were correspondingly denoted as S and H. Among reticular band models, only the results with an AR of 5 were represented because the trend was equivalent for all AR values, as described in the plots of Fig. 16. Interestingly, FEA results highlight major differences in stress and strain distributions, depending on the band array, as well as the AR.

Firstly, CB material with a columnar band array demonstrated a more severe shear stress and plastic shear strain state within the soft layers as compared to FB material with a reticular band array (*cf.* Fig. 16 (a) and (b)), despite generating a homogeneous distribution of shear stress across the CB material. The higher stress and plastic strain concentrations within the soft regions are likely to significantly reduce the fatigue limit of the CB material, even under equivalent applied stress levels. On the other hand, the FB material with a reticular band array displayed less severe mechanical states, perhaps attributable to the microstructurally-induced plastic constraints by the hard layers imposed on the soft layers, as reported by Chan and Lee [43]. In other words, while plastic strains build up in the soft layers at the onset of yielding, the hard layers remain elastic and induce a constraint on the soft layers from easy plastic deformation. In addition, FEA results indicated that varying ARs considerably affect the localization and magnitude of stress and plastic strain within the reticular band materials, *i.e.*, lower ARs reduce stress and plastic strain within soft layers. This result is likely due to the increased amount of surrounding hard layers which induce microstructural constraints on the soft layers.

The preceding analyses underscore the critical role of microstructural configuration on the fatigue strength of the materials. Columnar band morphologies impose major degradation on the fatigue resistance due to intense plastic strain concentrations in soft layers. In contrast, reticular band morphologies offer a better fatigue performance under cyclic torsional loading conditions. This study emphasizes the necessity for comprehensive material design strategies that take into account specific morphological characteristics, so as to optimize fatigue strength in engineering applications where cyclic torsional loading is prevalent. Further work is needed to investigate the combined effects of grain size, band spacing, and band array to better understand their collective impact on fatigue strength. Additional experiments will also be

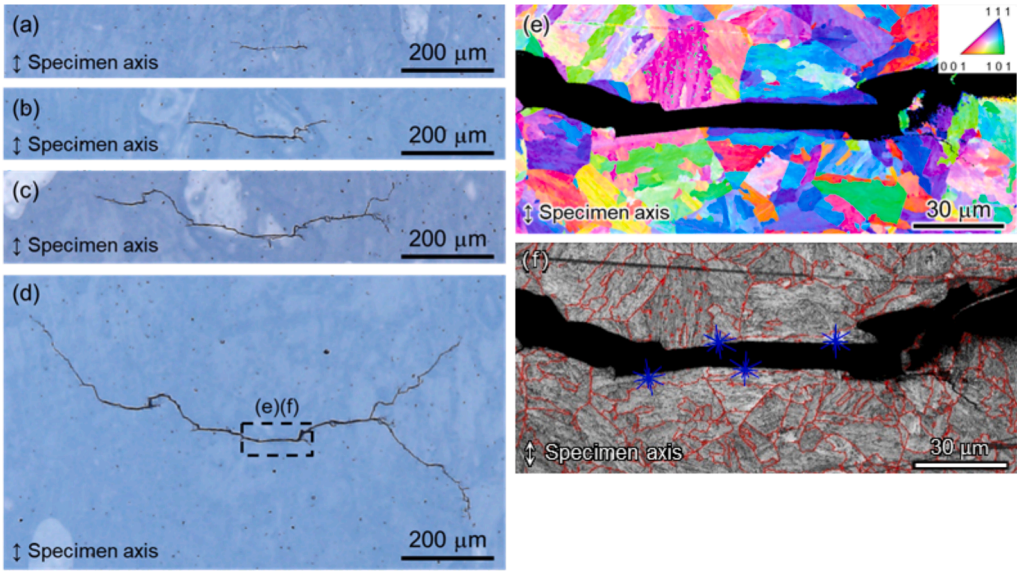

Fig. 13. Crack-propagation behavior and microstructure in the vicinity of the CB crack, tested at τ_a = 280 MPa: (a) ~ (d) Optical micrographs; (e) IPF map; (f) GB map.

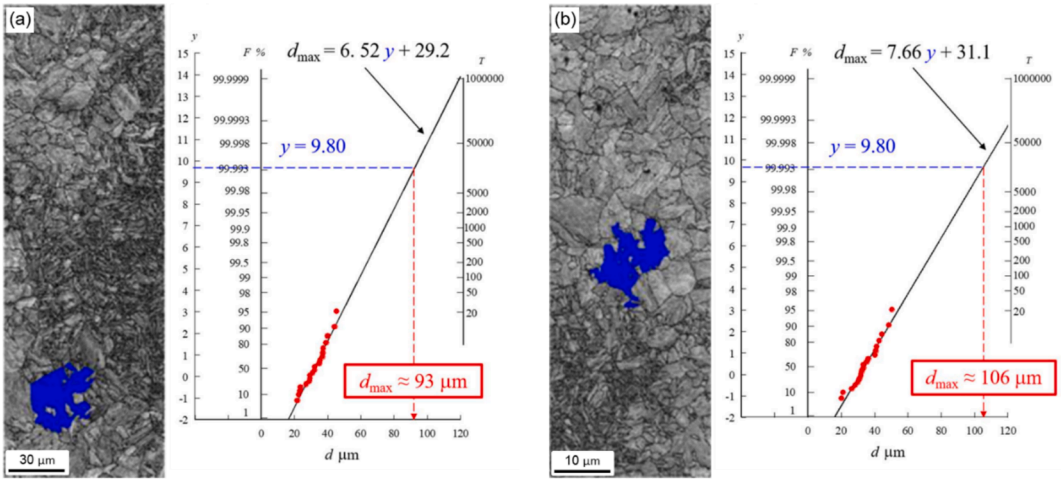

Fig. 14. An example of sampling of the maximum grain size using the EBSD technique and the resulting extreme value distribution of the maximum grain size in (a) CB and (b) FB samples.

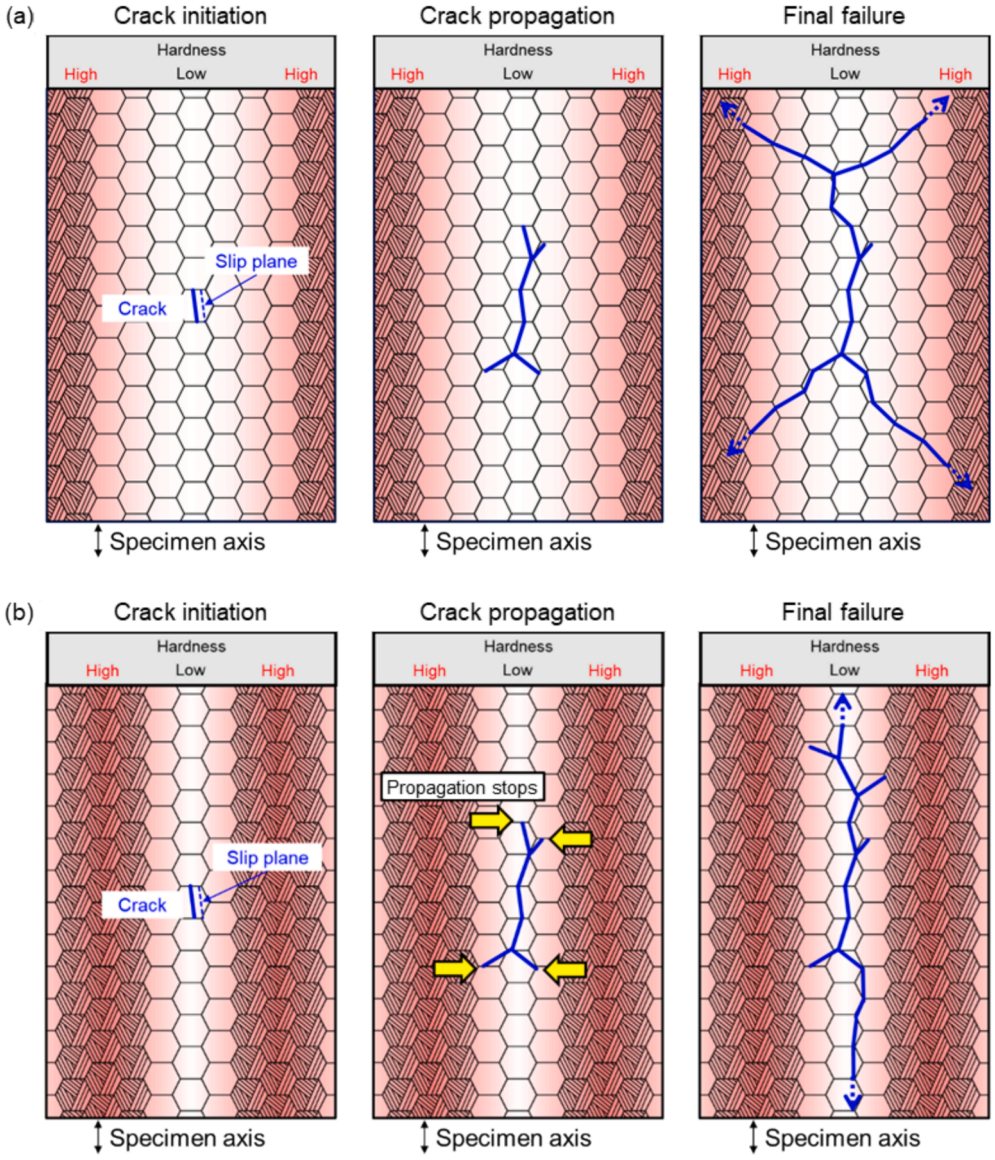

Fig. 15. Schematics of crack-initiation and −propagation behaviors in (a) CB and (b) FB materials.

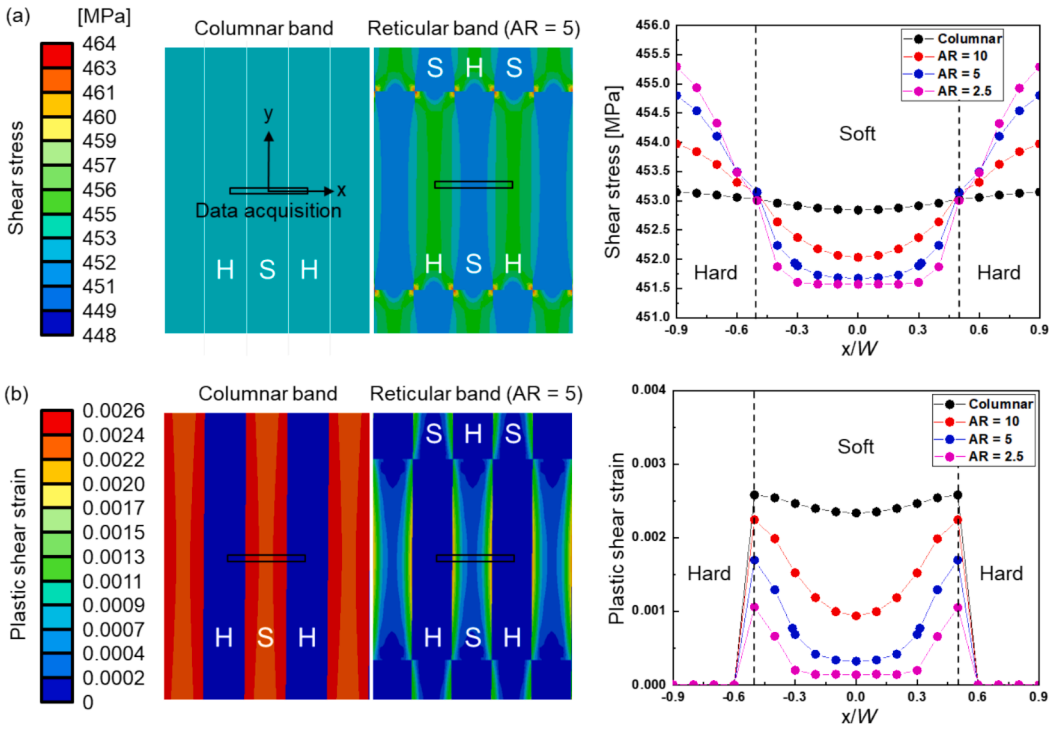

Fig. 16. FEA results: (a) shear stress; (b) plastic shear strain.

necessary to fully characterize the *S-N* data and precisely define the fatigue limit. Our future research will adopt a more integrated approach, likely involving advanced FEA techniques and a more extensive dataset, to quantify the interaction between these factors and their influence on fatigue resistance.

5. Conclusions

The present study investigated the dominant factors influencing the fatigue limit of bainitic steels with potential applications in marine diesel engine shafts. Torsional fatigue tests were conducted on two bainitic steels with similar Vickers hardness (*HV*) but different band morphologies: a coarse band (CB) material with a columnar band structure and $HV = 329$, along with a fine band (FB) material with a reticular band structure and $HV = 314$. Based on macro- and microscopic observations as well as finite element analysis, the following conclusions were established:

1. Despite the similar average *HV* values and comparable banded microstructures with coarse-grained and fine-grained regions, the FB material exhibited a 30 % higher torsional fatigue limit than the CB material.
2. In both the CB and FB materials, cracks primarily initiated in the coarse-grained regions, registering hardness values approximately 100 units lower than in the fine-grained regions.
3. One of the primary factors influencing the variation in torsional fatigue limits between the CB and FB materials was identified as the width of the banded microstructure. The narrower bands in the FB material provided higher resistance to branched, Mode I cracks; the fatigue limit of the FB material was therefore governed by the threshold condition for crack propagation. On the contrary, in the CB material with the wider bands, the fatigue limit was determined by the threshold condition for crack initiation, leading to a lower fatigue limit.
4. Band array can be considered to be another critical factor. The band structure in the CB material was rather columnar, whereas that of the FB material was more reticular. Finite element analysis revealed that, compared to the reticular band, the columnar band array led to a more severe stress and strain distribution within the soft layers. This was due to fewer constraints on plastic deformation from the surrounding hard layers.

CRediT authorship contribution statement

Soma Yoshimura: Writing – review & editing, Validation, Methodology, Investigation. **Kentaro Wada:** Writing – review & editing, Validation, Methodology, Investigation. **Sungcheol Park:** Writing – original draft, Visualization, Validation, Investigation. **Hisao Matsunaga:** Writing – review & editing, Validation, Supervision, Conceptualization.

Declaration of competing interest

The authors declare that they have no known competing financial interests or personal relationships that could have appeared to influence the work reported in this paper.

Acknowledgments

This work was financially supported by the collaborative research program between Japan Casting & Forging Corporation and Kyushu University. The authors wish to especially thank Dr. Yoshihiro Ohkomori, Ms. Tomoko Yamamoto and Mr. Michiaki Fukuya of Japan Casting & Forging Corporation for their dedicated contributions and valuable discussions.

Data availability

Data will be made available on request.

References

[1] Aakko-Saksa PT, Lehtoranta K, Kuittinen N, Järvinen A, Jalkanen J-P, Johnson K, et al. Reduction in greenhouse gas and other emissions from ship engines: Current

trends and future options. Prog Energy Combust Sci 2023;94:101055. https://doi.org/10.1016/j.pecs.2022.101055.
[2] Long XY, Zhang FC, Kang J, Lv B, Shi XB. Low-temperature bainite in low-carbon steel. Mater Sci Eng, A 2014;594:344–51. https://doi.org/10.1016/j.msea.2013.11.089.
[3] Li Y, Zhang F, Chen C, Lv B, Yang Z, Zheng C. Effects of deformation on the microstructures and mechanical properties of carbide-free bainitic steel for railway crossing and its hydrogen embrittlement characteristics. Mater Sci Eng, A 2016;651:945–50. https://doi.org/10.1016/j.msea.2015.09.117.
[4] Wang YH, Zhang FC, Wang TS. A novel bainitic steel comparable to maraging steel in mechanical properties. Scr Mater 2013;68(9):763–6. https://doi.org/10.1016/j.scriptamat.2012.12.031.
[5] De-Castro D, Eres-Castellanos A, Vivas J, Caballero FG, San-Martín D, Capdevila C. Morphological and crystallographic features of granular and lath-like bainite in a low carbon microalloyed steel. Mater Charact 2022;184:111703. https://doi.org/10.1016/j.matchar.2021.111703.
[6] Wang TS, Li XY, Zhang FC, Zheng YZ. Microstructures and mechanical properties of 60Si2CrVA steel by isothermal transformation at low temperature. Mater Sci Eng, A 2006;438–440:1124–7. https://doi.org/10.1016/j.msea.2006.02.077.
[7] Sourmail T, Smanio V. Optimisation of the mechanical properties of air cooled bainitic steel components through tailoring of the transformation kinetics. Mater Sci Eng, A 2013;582:257–61. https://doi.org/10.1016/j.msea.2013.06.040.
[8] Wang K, Tan Z, Gao G, Gao B, Gui X, Misra RDK, et al. Microstructure-property relationship in bainitic steel: The effect of austempering. Mater Sci Eng, A 2016;675:120–7. https://doi.org/10.1016/j.msea.2016.08.026.
[9] Wang W, Wang S, Zhang X, Chen F, Xu Y, Tian Y. Process parameter optimization for selective laser melting of Inconel 718 superalloy and the effects of subsequent heat treatment on the microstructural evolution and mechanical properties. J Manuf Processes 2021;64:530–43. https://doi.org/10.1016/j.jmapro.2021.02.004.
[10] Marinelli MC, Balbi M, Krupp U. Influence of plastic deformation in fatigue crack behavior in bainitic steel. Int J Fatigue 2021;143:106014. https://doi.org/10.1016/j.ijfatigue.2020.106014.
[11] Kang J, Zhang FC, Long XY, Lv B. Low cycle fatigue behavior in a medium-carbon carbide-free bainitic steel. Mater Sci Eng, A 2016;666:88–93. https://doi.org/10.1016/j.msea.2016.03.077.
[12] Long XY, Zhang FC, Zhang CY. Effect of Mn content on low-cycle fatigue behaviors of low-carbon bainitic steel. Mater Sci Eng, A 2017;697:111–8. https://doi.org/10.1016/j.msea.2017.04.089.
[13] Marinelli MC, Alvarez-Armas I, Krupp U. Cyclic deformation mechanisms and microcracks behavior in high-strength bainitic steel. Mater Sci Eng, A 2017;684:254–60. https://doi.org/10.1016/j.msea.2016.12.018.
[14] Zhang FC, Long XY, Kang J, Cao D, Lv B. Cyclic deformation behaviors of a high strength carbide-free bainitic steel. Mater Des 2016;94:1–8. https://doi.org/10.1016/j.matdes.2016.01.024.
[15] Murakami Y, Endo M. Quantitative evaluation of fatigue strength of metals containing various small defects or cracks. Eng Fract Mech 1983;17(1):1–15. https://doi.org/10.1016/0013-7944(83)90018-8.
[16] Murakami Y, Endo M. Effects of defects, inclusions and inhomogeneities on fatigue strength. Int J Fatigue 1994;16(3):163–82. https://doi.org/10.1016/0142-1123(94)90001-9.
[17] Kevinsanny OS, Takakuwa O, Ogawa Y, Okita K, Funakoshi Y, et al. Effect of defects on the fatigue limit of Ni-based superalloy 718 with different grain sizes. Fatigue Fract Eng Mater Struct 2019;42(5):1203–13. https://doi.org/10.1111/ffe.12989.
[18] Schönbauer BM, Mayer H. Effect of small defects on the fatigue strength of martensitic stainless steels. Int J Fatigue 2019;127:362–75. https://doi.org/10.1016/j.ijfatigue.2019.06.021.
[19] Åman M, Wada K, Matsunaga H, Remes H, Marquis G. The influence of interacting small defects on the fatigue limits of a pure iron and a bearing steel. Int J Fatigue 2020;135:105560. https://doi.org/10.1016/j.ijfatigue.2020.105560.
[20] Nayeb-Hashemi H, McClintock FA, Ritchie RO. Effects of friction and high torque on fatigue crack propagation in Mode III. Metall Trans A 1982;13:2197–204. https://doi.org/10.1007/BF02648390.
[21] Tschegg EK. Mode III and Mode I fatigue crack propagation behaviour under torsional loading. J Mater Sci 1983;18:1604–14. https://doi.org/10.1007/BF00542053.
[22] Tschegg EK. Sliding mode crack closure and mode III fatigue crack growth in mild steel. Acta Metall 1983;31(9):1323–30. https://doi.org/10.1016/0001-6160(83)90003-2.
[23] Okazaki S, Wada K, Matsunaga H, Endo M. The influence of static crack-opening stress on the threshold level for shear-mode fatigue crack growth in bearing steels. Eng Fract Mech 2017;174:127–38. https://doi.org/10.1016/j.engfracmech.2016.12.007.
[24] Tanaka Y, Okazaki S, Ogawa Y, Endo M, Matsunaga H. Fatigue limit of Ni-based superalloy 718 relative to the shear-mode crack-growth threshold: A quantitative evaluation considering the influence of crack-opening and -closing stresses. Int J Fatigue 2021;148:106228. https://doi.org/10.1016/j.ijfatigue.2021.106228.
[25] Pokluda J, Vojtek T, Hohenwarter A, Pippan R. Effects of microstructure and crystallography on crack path and intrinsic resistance to shear-mode fatigue crack growth. Frat Integrita Strutt 2015;9(34):142–9. https://doi.org/10.3221/IGF-ESIS.34.15.
[26] Park S, Tanaka Y, Okazaki S, Funakoshi Y, Kawashima H, Matsunaga H. Role of grain boundaries and precipitates in small, fatigue crack-growth resistance of additively-manufactured, Ni-based superalloy 718 under torsional cyclic loading. Mater Lett 2023;350:134844. https://doi.org/10.1016/j.matlet.2023.134844.
[27] Furuhara T, Kawata H, Morito S, Maki T. Crystallography of upper bainite in Fe-Ni-C alloys. Mater Sci Eng, A 2006;431(1–2):228–36. https://doi.org/10.1016/j.msea.2006.06.032.
[28] Siwecki T, Eliasson J, Lagneborg R, Hutchinson B. Vanadium Microalloyed Bainitic Hot Strip Steels. ISIJ Int 2010;50(5):760–7. https://doi.org/10.2355/isijinternational.50.760.
[29] Hu H, Xu G, Zhou M, Yuan Q. Effect of Mo content on microstructure and property of low-carbon bainitic steels. Metals 2016;6(8):173. https://doi.org/10.3390/met6080173.
[30] Ali M, Nyo T, Kaijalainen A, Hannula J, Porter D, Kömi J. Influence of chromium content on the microstructure and mechanical properties of thermomechanically hot-rolled low-carbon bainitic steels containing niobium. Appl Sci 2020;10(1):344. https://doi.org/10.3390/app10010344.
[31] Murakami Y. Metal fatigue: Effects of Small Defects and Nonmetallic Inclusions. 2nd Edition. UK: Academic Press; 2019.
[32] Zhai T, Wilkinson AJ, Martin JW. A crystallographic mechanism for fatigue crack propagation through grain boundaries. Acta Mater 2000;48(20):4917–27. https://doi.org/10.1016/S1359-6454(00)00214-7.
[33] Park S, Tanaka Y, Okazaki S, Funakoshi Y, Kawashima H, Matsunaga H. Inferior fatigue resistance of additively-manufactured Ni-based superalloy 718 and its dominating factor. Int J Fatigue 2023;176:107801. https://doi.org/10.1016/j.ijfatigue.2023.107801.
[34] Ruijie Z, Chunlei Z, Bo L, Peijun Z, Guhui G, Yongqiang Y, et al. Effect of non-uniform microstructure on rolling contact fatigue performance of bainitic rail steel. Int J Fatigue 2022;159:106795. https://doi.org/10.1016/j.ijfatigue.2022.106795.
[35] Ono Y, Yuri T, Nagashima N, Ogata T, Nagao N. Effect of microstructure on high-cycle fatigue properties of Alloy718 plates. IOP Conf Ser: Mater Sci Eng 2015;102:012001. https://doi.org/10.1088/1757-899X/102/1/012001.
[36] Romano S, Brückner-Foit A, Brandão A, Gumpinger J, Ghidini T, Beretta S. Fatigue properties of AlSi10Mg obtained by additive manufacturing: Defect-based modelling and prediction of fatigue strength. Eng Fract Mech 2018;187:165–89. https://doi.org/10.1016/j.engfracmech.2017.11.002.
[37] Linder J, Axelsson M, Nilsson H. The influence of porosity on the fatigue life for sand and permanent mould cast aluminium. Int J Fatigue 2006;28(12):1752–8. https://doi.org/10.1016/j.ijfatigue.2006.01.001.
[38] Fischer C, Schweizer C. Experimental investigation of the damage characteristics of two cast aluminium alloys: Part III – Influence of the local microstructure and initial defect size on the fatigue properties. Int J Fatigue 2021;152:106388. https://doi.org/10.1016/j.ijfatigue.2021.106388.
[39] Akiniwa Y, Stanzl-Tschegg S, Mayer H, Wakita M, Tanaka K. Fatigue strength of spring steel under axial and torsional loading in the very high cycle regime. Int J Fatigue 2008;30(12):2057–63. https://doi.org/10.1016/j.ijfatigue.2008.07.004.
[40] Kevinsanny OS, Takakuwa O, Ogawa Y, Funakoshi Y, Kawashima H, et al. Defect tolerance and hydrogen susceptibility of the fatigue limit of an additively manufactured Ni-based superalloy 718. Int J Fatigue 2020;139:105740. https://doi.org/10.1016/j.ijfatigue.2020.105740.
[41] Endo M, Yanase K. Crack path and threshold condition for small fatigue crack growth in annealed carbon steels under fully-reversed torsional loading. Int J Fatigue 2019;125:112–21. https://doi.org/10.1016/j.ijfatigue.2019.03.027.
[42] Erdogan F, Sih GC. On the crack extension in plates under plane loading and transverse shear. J Basic Eng 1963;85(4):519–25. https://doi.org/10.1115/1.3656897.
[43] Chan KS, Lee YD. Effects of deformation-induced constraint on high-cycle fatigue in Ti alloys with a duplex microstructure. Metall Mater Trans A 2008;39:1665–75. https://doi.org/10.1007/s11661-008-9540-3.